




Shape influence of β -MnO₂ on catalytic activity in the oxygen reduction reaction in alkaline media

Influencia de la forma del β -MnO₂ sobre la actividad catalítica en la reacción de reducción de oxígeno en medios alcalinos

I. Cruz-Reyes ^a, R.M. Félix-Navarro ^a, B. Trujillo-Navarrete ^{a,*}

^a Tecnológico Nacional de México/IT. Tijuana. Centro de Graduados e Investigación en Química. Blvd. Alberto Limón Padilla s/n Col. Otay Tecnológico, Tijuana, B.C. México.

Abstract

Rutile-phase β -MnO₂ nanostructures were produced using the hydrothermal method. The two types of nanostructures were compared: single nanorods and the hierarchical architecture of a dandelion flower-like shape. The morphology was examined through scanning/transmission electron microscopy (SEM/TEM), the Rietveld refinement technique, and surface area analysis, while the oxidation states were determined using X-ray Photoelectron Spectroscopy-Ultraviolet Photoelectron Spectroscopy (XPS-UPS). Both nanostructures were evaluated as catalysts for the oxygen reduction reaction (ORR) in alkaline environments. The results suggest that introducing shape increased the specific surface area and the Mn⁴⁺/Mn³⁺ ratio. This variation can be attributed to the microstructural changes. The ORR was facilitated by a four-electron mechanism, increasing current density. This enhancement was observed in rod-shaped and dandelion-shaped structures as well. Hydrogen peroxide (H₂O₂) production rates were determined using a rotating ring-disk electrode (RRDE), which was less than 20% in dandelions than in nanorods. This study enhances our understanding of β -MnO₂ catalysts and highlights their potential for energy conversion.

Keywords: Manganese oxide, the oxygen reduction reaction (ORR), nanorods, dandelions, catalysts.

Resumen

Las nanoestructuras de β -MnO₂ en fase rutilo se produjeron utilizando el método hidrotermal. Se compararon dos nanoestructuras: nanovarillas individuales y la arquitectura jerárquica similar a una flor de diente de león. Las dos morfologías se examinaron mediante SEM/TEM, la técnica de refinamiento de Rietveld y análisis de área de superficie, mientras que los estados de oxidación se determinaron mediante XPS-UPS. Ambas nanoestructuras fueron evaluadas como catalizadores para la ORR en ambientes alcalinos. Los resultados sugieren que la introducción de forma aumentó la superficie específica y la relación Mn⁴⁺/Mn³⁺. Esta variación se puede atribuir a los cambios microestructurales. La ORR fue facilitada por un mecanismo de 4e⁻, aumentando la densidad de corriente. Esta mejora se observó en las estructuras con forma de varillas y diente de león. Las tasas de producción de peróxido de hidrógeno (H₂O₂) se determinó utilizando un electrodo de disco de anillo giratorio (RRDE), la cual fue menor al 20% en el diente de león en comparación con las nanovarillas. Este estudio permite mejorar nuestra comprensión de los catalizadores de β -MnO₂ y destaca su potencial en la conversión de energía.

Palabras Clave: Óxido de manganeso, reacción de reducción de oxígeno (ORR), nanobarras, dientes de león, catalizadores.

1. Introduction

Due to their favorable chemical and physical properties, transition metal oxides (TMOs) have gained significant attention from researchers in recent years (Balan et al., 2013;

Lübke et al., 2018; Malkhandi et al., 2013). TMOs are essential in several technical applications, such as catalysts, adsorption, and device applications (Arges et al., 2010; Cui et al., 2020; C.-G. Han et al., 2017). Manganese oxide, a TMO, is significant in different fields of technology because of its

*Autor para la correspondencia: balter.trujillo@tectijuana.edu.mx

Correo electrónico: ivan.cruz19@tectijuana.edu.mx (Iván Cruz-Reyes), rmfelix2003@yahoo.com.mx (Rosa María Félix-Navarro), balter.trujillo@tectijuana.edu.mx (Balter Trujillo-Navarrete).

various oxidation states (+2, +3, and +4) and polymorphisms (e.g., α -MnO₂, γ -MnO₂, δ -MnO₂, and λ -MnO₂).

Investigating polymorphism of MnO₂ has been a topic of academic research ever since they were discovered as

enhancers of energy storage in batteries and renewable energy systems. Also, the β - MnO_2 catalysts have gained attention due to their reliability at room temperature, cost-effectiveness, and high ORR activity, making them potentially suitable for use in anion exchange membrane fuel cells (AEMFC) (Ferriday & Middleton, 2021; Gottesfeld et al., 2018; Venkata Swetha et al., 2018). Many studies have shown that the electrochemical performance of manganese oxide is significantly influenced by its structure, underscoring the pressing need for successful strategies for controlling its structure (Cheng et al., 2010; Lima et al., 2006; Stoerzinger et al., 2015). The catalytic activity of β - MnO_2 is influenced by factors such as the microstructure on its surface, the presence or absence of oxygen vacancies (OVs), and the oxidation states (Gu et al., 2019; Ryabova et al., 2016; Zhang et al., 2016).

Li et al. (2021) discovered that an increase in the concentration of Mn^{3+} and oxygen vacancies (OVs) could enhance the catalytic activity of β - MnO_2 in ORR (Li et al., 2021). However, the effect of morphology variation, microstructure, and the rate of Mn^{3+} or OVs still needs to be clarified (Arandiyan et al., 2013; Huang et al., 2014). This research studies two types of rutile-phase β - MnO_2 nanostructures: rods and controlled hierarchical rutile MnO_2 architectures) with a dandelion flower-like shape. This study aims to analyze the changes in microstructure and surface features associated with these nanostructures and to examine their effect on the presence or absence of Mn^{3+} and OVs. Furthermore, this investigation seeks to establish a relationship between these structural properties and the catalytic performance of the two nanostructures in ORR.

2. Experimental

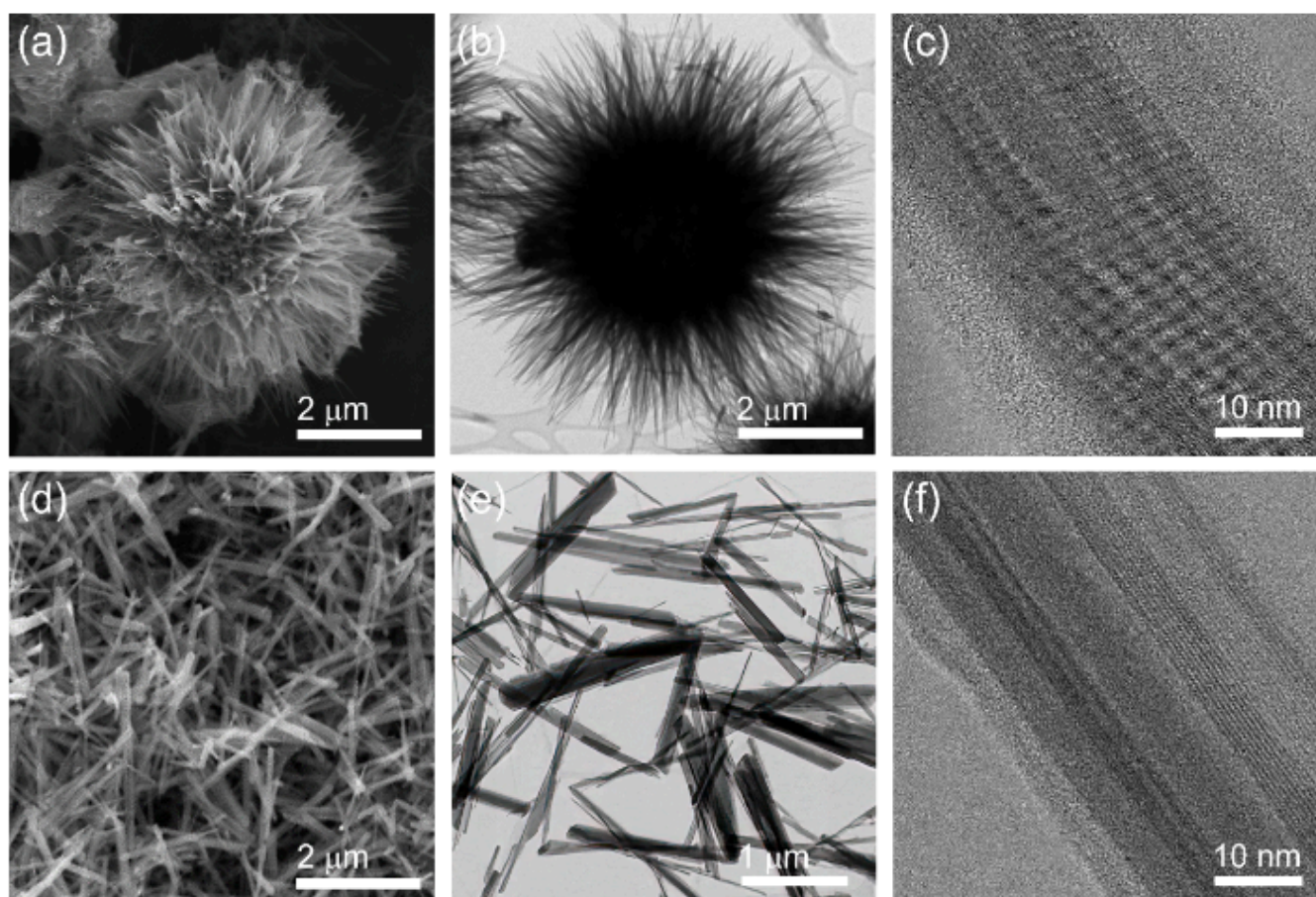
All the reagents used in this study were obtained from Sigma-Aldrich® and were used in their original state without any alterations. The reagents used in the study included potassium permanganate (K_2MnO_4 , 99.9%), manganese sulfate ($\text{MnSO}_4 \cdot \text{H}_2\text{O}$, 99.9%), potassium persulfate ($\text{K}_2\text{S}_2\text{O}_8$, 99.9%), potassium sulfate (K_2SO_4 , 99.9%), and methanol (CH_3OH , 99.8%). All the aqueous solutions were prepared using MilliQ® quality water ($18 \text{ M}\Omega \cdot \text{cm}^{-1}$, Millipore®), which was obtained from a deionizer system (Thermo Scientific™, Barnstead™ Pacific™ TII).

Two different morphologies of rutile-phase β - MnO_2 were synthesized through the hydrothermal method. The first was rods produced by mixing 1.0 mM of K_2MnO_4 and 1.0 mM of MnSO_4 in 30 mL of H_2O . The blend was stirred continuously for 0.5 hours at room temperature, then transferred to a Teflon® vial and placed inside a stainless-steel autoclave reactor. The reactor was heated in a convection oven at 120°C for 12.0 hours. The brown-dark precipitate was washed using a mixture of ethanol and water and dried at 60°C overnight.

The second morphology was dandelion flowers, which were synthesized using the same technique as the rods, except for the composition of the initial precursor solution. The modified solution consisted of 2.0 mmol of $\text{K}_2\text{S}_2\text{O}_8$, 2.0 mmol of K_2SO_4 , and 1.0 mmol of $\text{MnSO}_4 \cdot \text{H}_2\text{O}$ dissolved in 2.0 M of H_2SO_4 (30 mL). The resulting nanostructures were then classified according to their respective shapes.

2.1. Physicochemical Characterization

Figure 1: β - MnO_2 shapes: (a-b) SEM images; (c-d) TEM images.



The two shapes were analyzed using an SEM (Tescan® Vega3) and a TEM (JEOL®, JEM-2200FS). The X-ray diffractometer (Bruker®, D8Advance) was used to verify the crystalline phase, utilizing a Cu $K\alpha$ X-ray source with a wavelength (λ) of 1.54 Å, operating at 40 kV and 40 mA. The FullProf program (Version 6.3) was used to study the X-ray diffraction (XRD) peak broadening in the Bragg-Brentano geometry configuration. The spectra were obtained using a step size of 0.010° and a step-time of 1 second, covering the range of 15 to 85 degrees of 2θ . It is worth noting that the collected spectra have no processing, such as smoothing or filtering. The PDF-4/Minerals database (2022) was used to identify the phases. The Rietveld refinement analysis was done using the pseudo-Voigt profile function proposed by Thompson-Cox-Hastings with the treatment of axial divergence in the FullProf software (V. 6.3). Also, the profile analysis from Rietveld refinement allowed the calculation of the average crystallite size by Whole Powder Pattern Fitting (WPPF), which fits the observed diffraction profile via a peak shape function based on the phase information. The powders were analyzed using surface area analyzers (Quantachrome® Autosorb) to determine the specific surface area (SSA) and pore size by analyzing N_2 -sorption isotherms. The chemical states on the surface of the two nanostructures were identified using an XPS-UPS System (SPECS® GmbH).

2.2. Electrochemical Characterization

We tested the two types of β - MnO_2 nanostructures in powder form for their catalytic-ink properties. The test was conducted in a three-electrode cell configuration, with a glassy carbon rotating disk electrode (RDE) as the working electrode, a Hg/HgO/NaOH 1 M reference electrode, and a Pt-coil as the counter-electrode. The RDE surface was modified by applying a catalytic ink consisting of 40 μ L. The ink was made by combining 2 mg of powder and 2 mg of functionalized MWCNT, individually dispersed in 550 μ L of ethanol and 150 μ L of Nafion® solution (Zapata-Fernández et

concentration of the β - MnO_2 ink. The catalytic activity of the ink for ORR was measured using linear sweep voltammetry (LSV) at various rotation speeds, namely 100, 250, 500, 750, 1000, and 1600 rpm. The LSV measurements were performed at a scan rate of $10 \text{ mV}\cdot\text{s}^{-1}$ in an electrolytic solution of sodium hydroxide (NaOH) with a concentration of 0.1 M. The solution was saturated with oxygen (O_2).

3. Result and discussion

Figure 1 shows the two synthesized forms: the hierarchical architecture of a dandelion flower-like shape and single rods. The micrometric and nanometric details can be observed from high-resolution SEM and bright-field TEM images. The average diameter of HRMA's is $5 \pm 0.88 \mu\text{m}$, as shown in Figures a and b. In contrast, the nanorods exhibit a diameter of $100 \pm 20 \text{ nm}$ and a length of $1.3 \pm 0.17 \mu\text{m}$, as illustrated in Figures d and e. TEM images also prove that the petals and bars have minuscule crystals forming the primary bars. Each nanorod has a diameter of around 9 nm, as shown in Figures c or f. The petals are composed of several uniform radial nanorods. Both structures exhibit a pristine and uniform surface devoid of nanoparticles or agglomerates.

The X-ray diffraction (XRD) patterns of the β - MnO_2 powders are displayed in Figure 2 a-b. The peak intensities indexation provided evidence supporting the classification of rutile-phase β - MnO_2 (JCPDS card numbers: 00-24-0735) as belonging to the tetragonal phase and space group $P_{42/mnm}$ (136). The profile's R-factor values were less than 10%. The lattice constants examination revealed an increase in the cell unit's volume (V) for the dandelion structure due to the corresponding increases in the cell dimensions a , b , and c .

The octahedral array investigation showed that the square base of the dandelion's bipyramid experienced a contraction. This contraction was mainly due to a decrease in the bond length between manganese (Mn) and oxygen (O) atoms at position 1 ($Mn-O_{(1)}$), whereas the bond length between Mn and O atoms at position 2 ($Mn-O_{(2)}$) remained relatively unchanged. Figure SI-1 illustrates the correlation between the experimental (Y_{calc}) and theoretical (Y_{obs}) peak profiles.

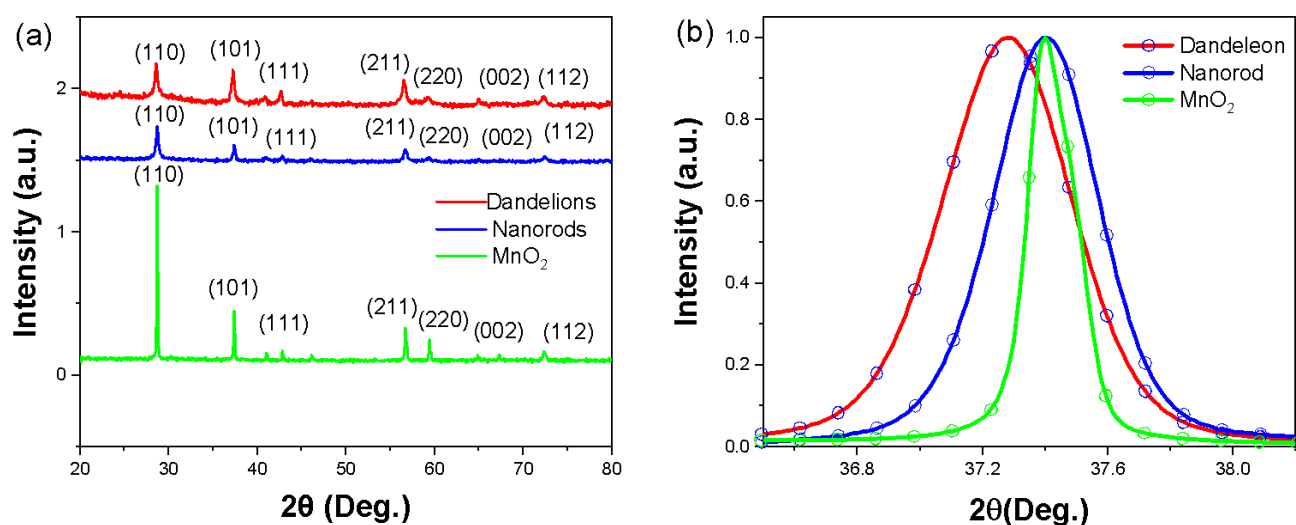
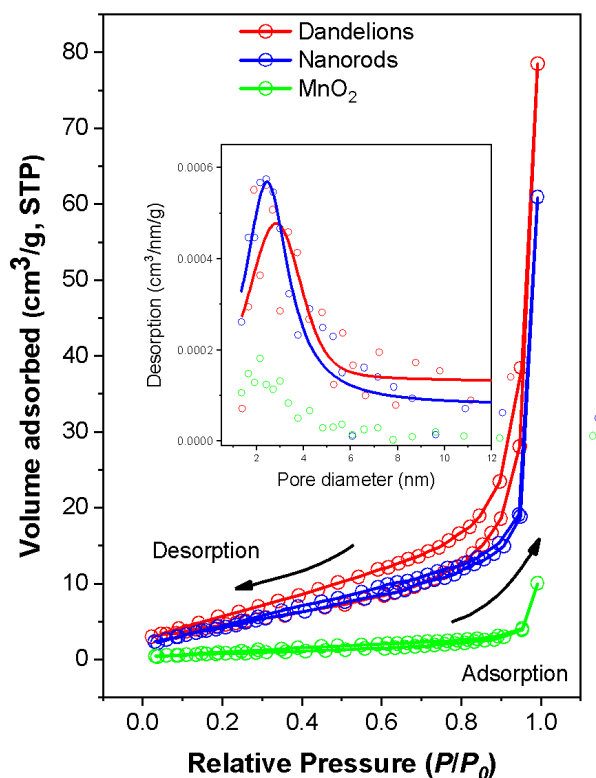


Figure 2: XRD patterns of the β - MnO_2 powders: (a) The indexing of the two shapes is consistent with the commercial material β - MnO_2 , and (b) the peak intensity (1 0 1).

al., 2017). The resulting solution contained a 30% (v/v)

The WPPF analysis application yielded valuable insights into the dandelion sample's crystallite size (D_v) and strain (τ). The analysis indicated a decrease in D_v along the (1 1 0) direction, while an increase was observed along the (0 0 1) direction. These changes in D_v were shown to be associated with a strain increment (τ).

Figure 3 displays the nitrogen isotherms recorded at a temperature of 77 K. As per the IUPAC classification (Sing, 1985), the isotherm can be classified as type IV based on the shape of the hysteresis loop within a relative pressure (P/P_0) range of 0.3-1.0. By analyzing the parallel sorption boundary curves shown in the figure, we can observe significant differences in the pore structure, which can be attributed to the extensive connectivity of pores in dandelions (Rojas et al., 2002). The inset of Figure 3 compares the narrow pore-size distribution. The variation in average pore diameter (D_{pore}) has resulted in a modification of the total pore volume (V_p),



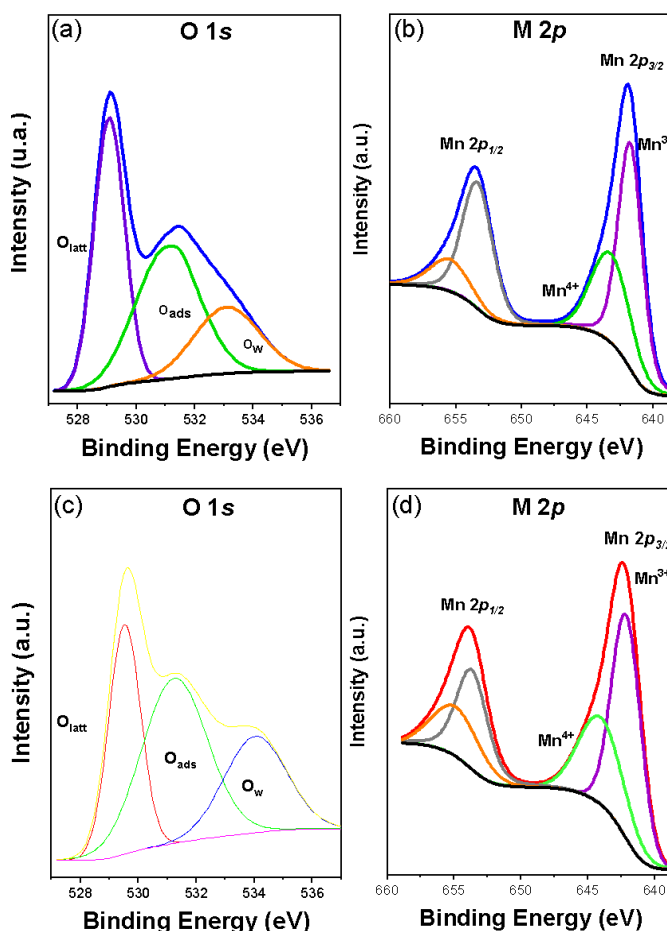
leading to a substantial increase of up to five times in the specific surface area (SSA) of nanocrystalline β -MnO₂.

Figure 3: N₂ sorption isotherms and BJH-PSD.

X-ray photoelectron spectroscopy (XPS) was used to investigate the nanostructure's chemical composition and the oxidation states of the metal. Three elements were observed in the full-scan spectrum of powders, as shown in Figure SI-2. The Mn 2p spectrum is shown in Figure 4, where Lorentzian peak-deconvolution analysis was performed. The study focused on two aspects: (1) the splitting of the Mn 2p spin-orbit doublet into Mn 2p_{3/2} (642 eV) and Mn 2p_{1/2} (653 eV) (Bocquet et al., 1992), and (2) the examination of the O

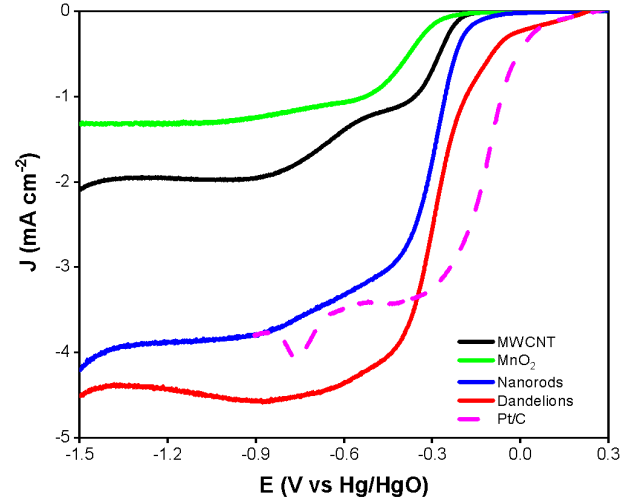
1s area, as depicted in Figure 4a and c, spanning from 526 eV to 538 eV (National Institute of Standards and Technology, 2000). The analysis of the Mn 2p_{3/2} core-level spectra revealed the two distinct initial states: Mn³⁺ [3d³] and Mn⁴⁺ [3d⁴], localized at energy levels of 641 eV (Mn³⁺) and 643 eV (Mn⁴⁺), respectively (S. W. Han et al., 2002). The energy difference between the two peaks was 11.9 electron volts (eV), which aligns with previous findings (Pinaud et al., 2011; Xie et al., 2014; Zhao et al., 2020).

The O 1s spectrum, shown in Figures 4b and 4d, exhibits three distinct peaks with intensities at 529 eV, 531 eV, and 533 eV. The peak at 529 eV corresponds to lattice oxygen (O_{latt}), while the peak at 531 eV is associated with oxide defects related to adsorbed-oxygen species (O_{ads}), such as O²⁻, O⁻, and OH. Lastly, the peak at 533 eV is attributed to adsorbed water (O_w) on the surface (Alexander et al., 2000). The variable ϕ is defined as the quotient of Mn⁴⁺/Mn³⁺, while



the variable ϕ represents the ratio O_{ads}/O_{latt}. The dandelion shape exhibited a notable disparity in the various shapes, with an ϕ value increase of up to 1.5 times and an ϕ value increase of up to 45% compared to rods. Table 1 provides a comprehensive summary of the physicochemical properties of the powders.

Figure 4: High-resolution XPS core-level spectra. Nanorods: (a) Mn 2p and (c) O 1s; and dandelions: (b) Mn 2p and (d) O 1s.



| | MWCNT | MnO ₂ | Nanorods | Dandelions | Pt/C |
|----------------------------------|-----------|------------------|-----------|------------|------|
| V_p (cm ³ /g) | 0.12 | 0.10 | 0.16 | | |
| $D_{v(110)}$ | 74(7) | 84(10) | 273(22) | | |
| e (10 ⁻³) | 7.1(1) | 6.2(1) | 1.3(1) | | |
| a (nm) | 0.4408(2) | 0.4402(3) | 0.4396(1) | | |
| c (nm) | 0.2879(1) | 0.2872(1) | 0.2871(0) | | |
| V (nm ³) | 0.0559 | 0.0556 | 0.0554 | | |
| Mn-O ₍₁₎ (Å) | 1.9 (4) | 1.9 (4) | 1.9 (3) | | |
| Mn-O ₍₂₎ (Å) | 1.9 (4) | 1.9 (5) | 1.8 (4) | | |
| φ | 1.52 | 0.60 | -- | | |
| ϕ | 1.51 | 1.03 | -- | | |
| Electrochemical: | | | | | |
| N | 4 | 4 | 3 | | |
| J_{lim} (mA·cm ⁻²) | -7.0231 | -5.2465 | -2.2951 | | |
| E_0 (V vs. RHE) | 0.8700 | 0.7600 | 0.7400 | | |
| $E_{1/2}$ (V vs. RHE) | 0.7400 | 0.6300 | 0.6300 | | |

We aimed to evaluate ORR's catalytic activities in an electrolyte containing oxygen-saturated 0.1 M NaOH. We employed the rotating disk and ring-disk electrode method for this purpose. Figure 5 shows the linear sweep voltammograms of β -MnO₂ nanorods and dandelions and the results obtained using the Pt/C catalyst, commercial MnO₂, and CNT for comparison. Our findings demonstrate that the electrocatalytic performance of nanorods and dandelions is superior to that of reference MnO₂ and MWCNT in the context of ORR. Notably, dandelions exhibit better catalytic activity than rods. Moreover, our results reveal that only Pt/C exhibits a superior half-wave potential among the tested catalysts.

Table 1 summarizes the kinetic characteristics of β -MnO₂ nanorods and dandelions compared to commercially available MnO₂. The commercial MnO₂ has a half-wave potential ($E_{1/2}$) of -0.410 V and a limiting current density (J_{lim}) of -1.29 mA/cm² at -1.0 V. When different morphologies are used, $E_{1/2}$ values shift towards more positive values, and there is an increase in J_{lim} . The experimental results show that nanorods have a half-wave potential ($E_{1/2}$) of -0.304 V and a limiting current density (J_{lim}) of -3.85 mA/cm². During the evaluation of dandelion blossoms, the measured current density (J_{lim}) increased from -3.85 mA/cm² to -4.54 mA/cm². They used a specified morphology for MnO₂, resulting in a threefold enhancement of J_{lim} and a shift of $E_{1/2}$ by over 100 mV towards more positive values. The Butler–Volmer equation was used, where their reduced function for small overpotentials conducts to linear Equation (1) that is used to calculate exchange current density (J_0) values for β -MnO₂ nanorods, dandelions and MnO₂ commercial at $|F\eta|$ "RT, as shown in Table 1.

$$\frac{\eta}{J} = \frac{RT}{J_0 F} \quad (1)$$

Table 1: Physicochemical and electrochemical parameters for β -MnO₂ shapes.

| | Dandelions | Nanorods | Commercial MnO ₂ |
|---------------------------|------------|-----------|-----------------------------|
| Physicochemical: | | | |
| d_w (nm) | 9 | 100(20) | -- |
| d_t (nm) | 5000(880) | 1300(170) | -- |
| f (dimensionless) | 555 | 13 | ≈ 1.0 |
| SSA (m ² /g) | 28.50 | 31.96 | 5.30 |
| D_{pore} (nm) | 28.5 | 21.3 | 20.5 |

In the micropolarization region of oxygen reduction and evolution reaction (ORR and OER), the overpotential is denoted by η . The current density is represented by J , while R is the universal gas constant (8.314 J mol⁻¹K⁻¹). T refers to the temperature of 298.15 K, and F is the constant Faraday, which has a value of 96,485 C mol⁻¹. Figure SI-3a illustrates the micro-polarization zone for ORR/OER. The value of J_0 for the MnO₂ commercial and β -MnO₂ nanorods were similar, with the former measuring 1.40×10^{-6} A/cm² and the latter measuring 1.92×10^{-6} A/cm². The β -MnO₂ dandelions, on the other hand, achieved a superior value of 3.75×10^{-5} A/cm².

Figure 5: Comparison of β -MnO₂ shapes on catalytic activity for ORR linear voltammograms recorded in O₂-saturated 0.1 M NaOH at 1600 rpm.

The Tafel plots are displayed in Figure SI-3b, depicting the Tafel slopes for ORR in two different β -MnO₂ morphologies. The Tafel slope for the dandelion-shaped β -MnO₂ is 61.0 mV/dec, whereas the nanorod-shaped β -MnO₂ has a Tafel slope of 73.9 mV/dec. These values suggest that the rate-determining step of the ORR is the transfer of the first electron, accompanied by less-than-ideal oxygen adsorption on the electrocatalyst, known as Temkin adsorption. The Tafel slopes increase to 149.5 mV/dec when using commercial MnO₂, indicating alterations in the rate-determining phase of the reaction, specifically towards the optimum adsorption of oxygen on the electrocatalyst, known as Langmuir adsorption. Cabot et al. (2012) documented similar alterations in the Tafel slope (Velázquez-Palenzuela et al., 2012).

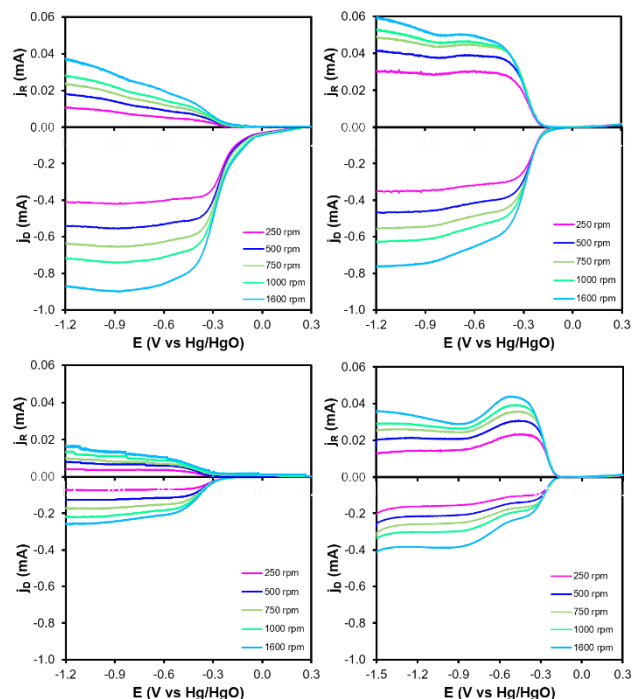


Figure 6: Hydrodynamic voltammograms for the ORR and H₂O₂ oxidation at a rotating glassy carbon disk coated with β-MnO₂ shapes: (a) Dandelions, (b) nanorods, (c) commercial MnO₂, (d) MWCNT and rotating Pt ring electrode respectively.

ORR is a complex process that involves the transfer of multiple electrons. It consists of several primary steps and the formation of various reaction intermediates. To determine the production rates of H₂O and H₂O₂, we can use the RRDE approach. This involves setting the ring's potential at 1.1 V, a value that limits the oxidation of H₂O₂ generated by the reduction of O₂ on the disc due to diffusion. Figure 6 displays the currents present in both the ring and the disk.

Figures SI-4a and SI-4b exemplify the creation of hydroperoxide in alkaline environments and the measurement of transferred electrons (*n*) during ORR. The production of H₂O₂ was calculated using Equation 2. In this context, *I_r* represents the ring current, *I_d* represents the disk current, and "N" means the collection efficiency (with a specific value of N = 0.25). The number of transferred electrons was determined using Equation 3.

$$H_2O_2\% = \frac{100 * \frac{2 * I_r}{N}}{I_d + \frac{I_r}{N}} \quad (2)$$

$$n = \frac{4 * I_d}{I_d + \frac{I_r}{N}} \quad (3)$$

β-MnO₂ dandelions produce less than 20% H₂O₂, and *n* is close to four. With β-MnO₂ nanorods, 50% of the oxygen is converted to H₂O₂, so *n* is approximately three.

To summarize, the results from the physicochemical analysis indicate that the flower-like hierarchical 3D-nanoarchitecture and rod create structural changes as the Mn-O₍₁₎ bond weakens. This alteration leads to the distortion of the irregular octahedral array and increased mobility for both the O atom and the electron density around the Mn atom in the unit cell. The radial contraction of the nanocrystal and

the elongation axial also increase the number of defects and modify the specific pore structure. These changes are likely linked to the increase in adsorbed-oxygen species, which suggests that the highest OV's sites on the β-MnO₂ surface experience an increase in the occurrence of Mn³⁺. As a result, the catalyst's performance is likely to improve due to the increase in catalytic sites through the restructuring of the β-MnO₂ shape. This adjustment can modify the ORR mechanism to 4e⁻, which requires less energy for the reaction to occur and can avoid the generation of H₂O₂.

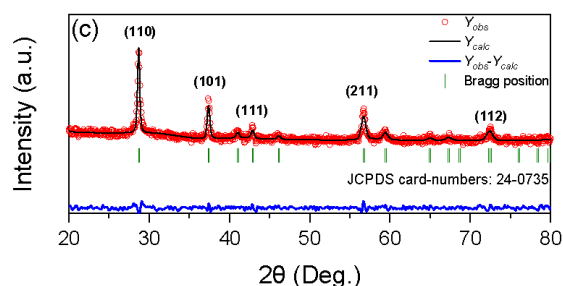
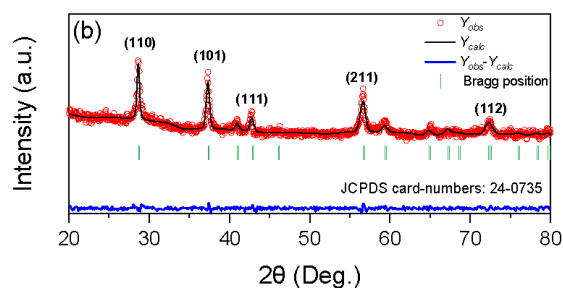
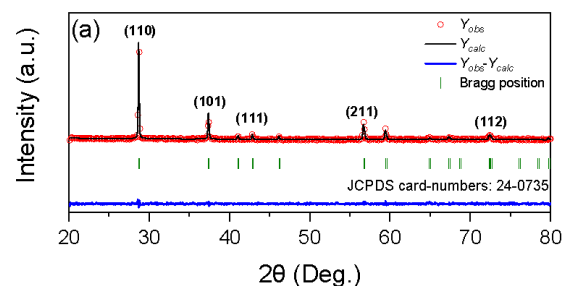
4. Conclusions

This study aimed to explore two different morphologies of rutile-phase β-MnO₂ and investigate how they affect the catalyst's electroactivity for ORR by altering the physicochemical characteristics. The study found that point defects, specifically oxygen vacancies (OVs) and manganese ions in the Mn³⁺ oxidation state, are critical in increasing the number of catalytic sites and improving the catalyst's performance. These materials promise potential application in alkaline exchange membrane fuel cells (AEMFC). These results interest researchers who are working on developing new materials using semiconductor nanostructures.

References

- Alexander, M. R., Thompson, G. E., & Beamson, G. (2000). Characterization of the oxide/hydroxide surface of aluminium using x-ray photoelectron spectroscopy: a procedure for curve fitting the O 1s core level. *Surface and Interface Analysis* 29(7), 468–477. DOI: 10.1002/1096-9918(200007)29:7<468::AID-SIA890>3.0.CO;2-V
- Arandiyán, H., Dai, H., Deng, J., Liu, Y., Bai, B., Wang, Y., Li, X., Xie, S., & Li, J. (2013). Three-dimensionally ordered macroporous La_{0.6}Sr_{0.4}MnO₃ with high surface areas: Active catalysts for the combustion of methane. *Journal of Catalysis* 307, 327–339. DOI: 10.1016/j.jcat.2013.07.013
- Arges, C. G., Ramani, V., & Pintauro, P. N. (2010). Anion exchange membrane fuel cells. In *Electrochemical Society Interface* 19(2), 31-35. DOI: 10.1149/2.F03102if
- Balan, L., Matei Ghimbeu, C., Vidal, L., & Vix-Guterl, C. (2013). Photoassisted synthesis of manganese oxide nanostructures using visible light at room temperature. *Green Chemistry* 15(8), 2191-2199. DOI: 10.1039/c3gc40487k
- Bocquet, A. E., Mizokawa, T., Saitoh, T., Namatame, H., & Fujimori, A. (1992). Electronic structure of 3d -transition-metal compounds by analysis of the 2p core-level photoemission spectra. *Physical Review B* 46(7), 3771–3784. DOI: 10.1103/PhysRevB.46.3771
- Cheng, F., Su, Y., Liang, J., Tao, Z., & Chen, J. (2010). MnO₂-Based Nanostructures as Catalysts for Electrochemical Oxygen Reduction in Alkaline Media †. *Chemistry of Materials* 22(3), 898–905. DOI: 10.1021/cm901698s
- Cui, C., Du, G., Zhang, K., An, T., Li, B., Liu, X., & Liu, Z. (2020). Co₃O₄ nanoparticles anchored in MnO₂ nanorods as efficient oxygen reduction reaction catalyst for metal-air batteries. *Journal of Alloys and Compounds* 814, 152239. DOI: 10.1016/j.jallcom.2019.152239.
- Ferriday, T. B., & Middleton, P. H. (2021). Alkaline fuel cell technology - A review. *International Journal of Hydrogen Energy* 46(35), 18489–18510. DOI: 10.1016/j.ijhydene.2021.02.203
- Gottesfeld, S., Dekel, D. R., Page, M., Bae, C., Yan, Y., Zelenay, P., & Kim,

- Y. S. (2018). Anion exchange membrane fuel cells: Current status and remaining challenges. *Journal of Power Sources* 375, 170–184. DOI: 10.1016/j.jpowsour.2017.08.010
- Gu, Y., Yan, G., Lian, Y., Qi, P., Mu, Q., Zhang, C., Deng, Z., & Peng, Y. (2019). MnIII-enriched α -MnO₂ nanowires as efficient bifunctional oxygen catalysts for rechargeable Zn-air batteries. *Energy Storage Materials* 23, 252–260. DOI: 10.1016/j.ensm.2019.05.006
- Han, C.-G., Zhu, C., Aoki, Y., Habazaki, H., & Akiyama, T. (2017). MnO/N-C anode materials for lithium-ion batteries prepared by cotton-templated combustion synthesis. *Green Energy & Environment* 2(4), 377–386. DOI: 10.1016/j.gee.2017.08.004
- Han, S. W., Lee, J. D., Kim, K. H., Song, H., Kim, W. J., Kwon, S. J., Lee, H. G., Hwang, C., Jeong, J. I., & Kang, J.-S. (2002). Electronic Structures of the CMR Perovskites R_{1-x}A_xMnO₃ (R = La, Pr; A = Ca, Sr, Ce) Using Photoelectron Spectroscopy. *Journal of the Korean Physical Society* 40(3), 501–510.
- Huang, M., Mi, R., Liu, H., Li, F., Zhao, X. L., Zhang, W., He, S. X., & Zhang, Y. X. (2014). Layered manganese oxides-decorated and nickel foam-supported carbon nanotubes as advanced binder-free supercapacitor electrodes. *Journal of Power Sources* 269, 760–767. DOI: 10.1016/j.jpowsour.2014.07.031
- Li, Z., Yang, Y., Releforts, A., Kong, X., Siso, G. M., Wickman, B., Kiros, Y., & Soroka, I. L. (2021). Tuning morphology, composition, and oxygen reduction reaction (ORR) catalytic performance of manganese oxide particles fabricated by γ -radiation induced synthesis. *Journal of Colloid and Interface Science* 583, 71–79. DOI: 10.1016/j.jcis.2020.09.011
- Lima, F. H. B., Calegario, M. L., & Ticianelli, E. A. (2006). Investigations of the catalytic properties of manganese oxides for the oxygen reduction reaction in alkaline media. *Journal of Electroanalytical Chemistry* 590(2), 152–160. DOI: 10.1016/j.jelechem.2006.02.029
- DOI: 10.1002/slct.201702514
- Malkhandi, S., Trinh, P., Manohar, A. K., Jayachandrababu, K. C., Kindler, A., Surya Prakash, G. K., & Narayanan, S. R. (2013). Electrochemical Activity of Transition Metal Oxide-Carbon Composites for Oxygen Reduction in Alkaline Batteries and Fuel Cells. *Journal of The Electrochemical Society* 160(9), F943–F952. DOI: 10.1149/2.109308jes
- National Institute of Standards and Technology. (2000). NIST X-ray Photoelectron Spectroscopy Database. NIST Standard Reference Database Number 20. DOI: 10.18434/T4T88K
- Pinaud, B. A., Chen, Z., Abram, D. N., & Jaramillo, T. F. (2011). Thin Films of Sodium Birnessite-Type MnO₂: Optical Properties, Electronic Band Structure, and Solar Photoelectrochemistry. *The Journal of Physical Chemistry C*, 115(23) 11830–11838. DOI: 10.1021/jp200015p
- Rojas, F., Kornhauser, I., Felipe, C., Esparza, J. M., Cordero, S., Domínguez, A., & Riccardo, J. L. (2002). Capillary condensation in heterogeneous mesoporous networks consisting of variable connectivity and pore-size correlation. *Physical Chemistry Chemical Physics* 4(11), 2346–2355. DOI: 10.1039/b108785a
- Ryabova, A. S., Napolskiy, F. S., Poux, T., Istomin, S. Y., Bonnefont, A., Antipin, D. M., Baranchikov, A. Y., Levin, E. E., Abakumov, A. M., Kéranguéven, G., Antipov, E. V., Tsirlina, G. A., & Savinova, E. R. (2016). Rationalizing the Influence of the Mn(IV)/Mn(III) Red-Ox Transition on the Electrocatalytic Activity of Manganese Oxides in the Oxygen Reduction Reaction. *Electrochimica Acta* 187(2016), 161–172. DOI: 10.1016/j.electacta.2015.11.012
- Sing, K. S. W. (1985). Reporting physisorption data for gas/solid systems with special reference to the determination of surface area and porosity (Recommendations 1984). *Pure and Applied Chemistry* 57(4), 603–619. DOI: 10.1351/pac198557040603
- Stoerzinger, K. A., Risch, M., Han, B., & Shao-Horn, Y. (2015). Recent Insights into Manganese Oxides in Catalyzing Oxygen Reduction Kinetics. *ACS Catalysis* 5(10), 6021–6031.



- Lübke, M., Sumboja, A., McCafferty, L., Armer, C. F., Handoko, A. D., Du, Y., McColl, K., Cora, F., Brett, D., Liu, Z., & Darr, J. A. (2018). Transition-Metal-Doped α -MnO₂ Nanorods as Bifunctional Catalysts for Efficient Oxygen Reduction and Evolution Reactions. *ChemistrySelect* 3(9), 2613–2622.

[DOI: 10.1021/acscatal.5b01444
 Velázquez-Palenzuela, A., Centellas, F., Brillas, E., Arias, C., Rodríguez, R. M., Garrido, J. A., & Cabot, P.-L. (2012). Kinetic effect of the ionomer on the oxygen reduction in carbon-supported Pt electrocatalysts. *International Journal of Hydrogen Energy* 37(23), 17828–17836.
 DOI: 10.1016/j.ijhydene.2012.09.090
 Venkata Swetha, J., Parse, H., Kakade, B., & Geetha, A. (2018). Morphology dependent facile synthesis of manganese oxide nanostructures for oxygen reduction reaction. *Solid State Ionics* 328(October), 1–7.
 DOI: 10.1016/j.ssi.2018.11.002
 Xie, S., Dai, H., Deng, J., Yang, H., Han, W., Arandiyán, H., & Guo, G. (2014). Preparation and high catalytic performance of Au/3DOM Mn₂O₃ for the oxidation of carbon monoxide and toluene. *Journal of Hazardous Materials* 279, 392–401.
 DOI: 10.1016/j.jhazmat.2014.07.033
 Zapata-Fernández, J. R., Gochi-Ponce, Y., Salazar-Gastélum, M. I., Reynoso-Soto, E. A., Paraguay-Delgado, F., Lin, S. W., & Félix-Navarro, R. M. (2017). Ultrasonic-assisted galvanic displacement synthesis of Pt-Pd/MWCNT for enhanced oxygen reduction reaction: Effect of Pt concentration. *International Journal of Hydrogen Energy* 42(15), 9806–9815.
 DOI: 10.1016/j.ijhydene.2017.02.057
 Zhang, B., Cheng, G., Lan, B., Zheng, X., Sun, M., Ye, F., Yu, L., & Cheng, X. (2016). Crystallization design of MnO₂ via acid towards better oxygen reduction activity. *CrystEngComm* 18(36), 6895–6902.
 DOI: 10.1039/C6CE01131D
 Zhao, X., Liu, X., Li, F., & Huang, M. (2020). MnO₂@NiO nanosheets@nanowires hierarchical structures with enhanced supercapacitive properties. *Journal of Materials Science* 55(6), 2482–2491.
 DOI: 10.1007/s10853-019-04112-4

Appendix A.

Figure SI-1: Rietveld refinement plots of β -MnO₂ powders: (a) Commercial β -MnO₂, rods, and (b) dandelion; Vertical bars (|) indicate the positions of the

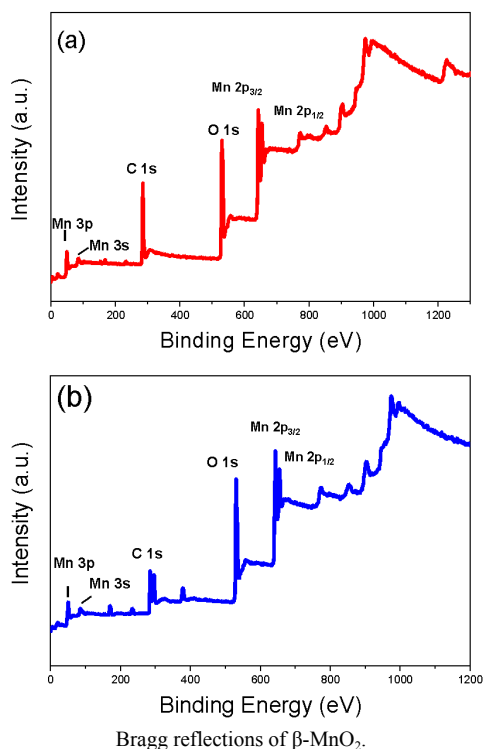


Figure SI-2: XPS survey of β -MnO₂: Mn 2p peaks were identified, showing a distance between peaks $\Delta \approx 11.9$ eV.

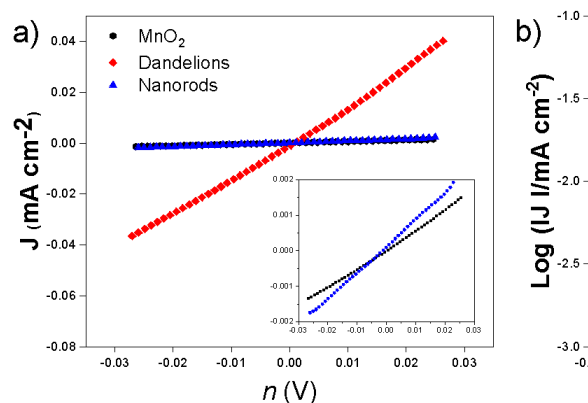


Figure SI-3: (a) ORR/OER micro-polarization region. (b) Tafel plots of

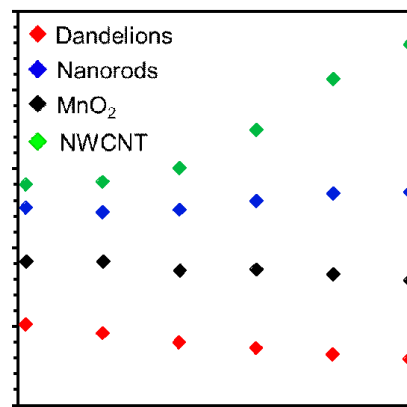


Figure SI-4: (a) Percentage of H₂O₂ and (b) the number of electrons transferred for Dandelions, Nanorods, MnO₂, and NWCNT.

